LA-UR-16-28780
Approved for public release; distribution is unlimited.

Title: Photon Next-Event Estimator Implementation in MCATK

Author(s): Sweezy, Jeremy Ed

Intended for: Report

Issued: 2016-11-14

Photon Next-Event Estimator Implementation in MCATK

Jeremy Sweezy

MCATK Team
XCP-3 Monte Carlo Methods, Codes, and Applications Group
Los Alamos National Laboratory

jsweezy@lanl.gov

LA-UR-16-XXXXX

Nov. 7, 2016, Revision 4

Abstract

A photon next-event fluence estimator at a point has been implemented in the Monte Carlo Application Toolkit (MCATK). The next-event estimator provides an expected value estimator for the flux at a point due to all source and collision events. An advantage of the next-event estimator over track-length estimators, which are normally employed in MCATK, is that flux estimates can be made in locations that have no random walk particle tracks. The next-event estimator allows users to calculate radiographs and estimate response for detectors outside of the modeled geometry. The next-event estimator is *not yet* accessable through the MCATK FlatAPI for C and Fortran. The next-event estimator in MCATK has been tested against MCNP6 using 5 suites of test problems. No issues were found in the MCATK implementation. One issue was found in the exclusion radius approximation in MCNP6. The theory, implementation, and testing are described in this document.

Theory of the Next-Event Estimator

The next-event estimator (NEE) at a point was first documented by Kalos [1]. This estimator is fundamentally different than the other Monte Carlo estimators offered in MCATK as the NEE does not require random walk particles to track through the cell containing the point. *Rather, the NEE at a point tallies the probability of a source or collision having a particle exit the event in the direction of the tally point multiplied by the probability of arriving at the point without collision.* The NEE is useful for simulating time-of-flight detectors, ex-core reactor instrumentation, and dose estimation at large distances from the source.

At every source and collision point, r, a contribution to the flux estimate at point, r', is performed (see Figure 1). The contribution to an estimator located at point r', due to a source or collision event, is

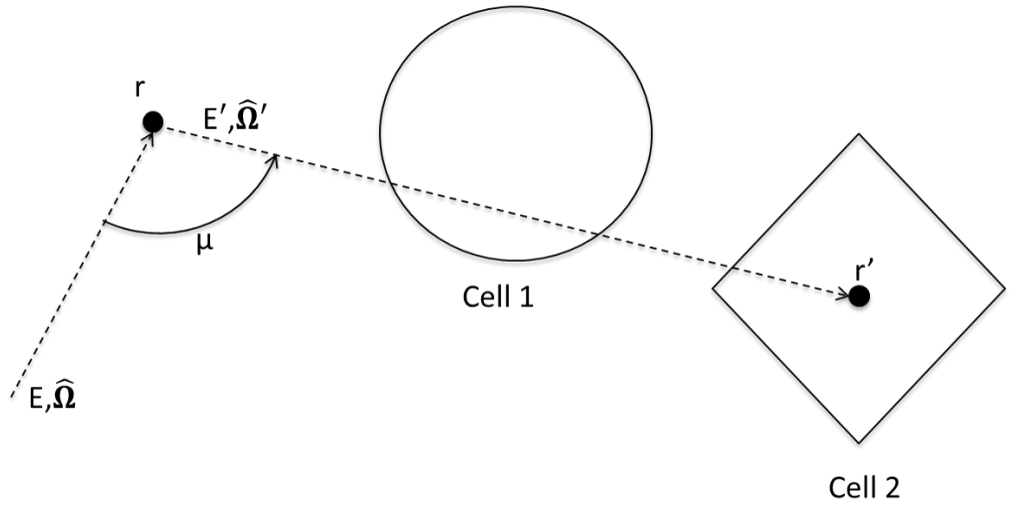

Figure 1: Next-event estimator at a point. Particle with energy, E, and direction, $\hat{\Omega}$, collides at point r. The flux at point r', in cell 2, is estimated by a NEE. The pseudo-particle leaving the collision toward the point r' has direction $\hat{\Omega}'$, scattering angle cosine μ, and energy, E'.

determined by:

$$\phi(Z,\mathcal{R},E',r') = w\,P(Z,\mathcal{R},E,r)\,\frac{p(Z,\mathcal{R},E\rightarrow E',\mu)}{2\pi|r-r'|^2}\exp\left(-\int_r^{r'}\Sigma_t(E',s)ds\right), \tag{1}$$

where E is the energy of the particle before collision, E' is the energy of the particle after scattering through angle cosine μ, r is the collision location, and r' is the detector location. $\phi(Z,\mathcal{R},E',r')$ is the contribution at point r' for collisions with isotope Z resulting in reaction $\mathcal{R}$ and resulting in a particle with energy E'. $p(Z,\mathcal{R},E\rightarrow E',\mu)$ is the probability of the particle scattering into angle cosine, μ, with resulting energy E', for reaction $\mathcal{R}$ of isotope Z given an incident energy E. The exiting energy E' is generally a function of the initial energy E and the scattering angle cosine μ. $|r-r'|$ is the distance between the collision or source point and the detector, $\Sigma_t(E',s)$ is the macroscopic cross section at energy E' and position s along the path between the collision point and the detector. The particle statistical weight is denoted as w. $P(Z,\mathcal{R},E,r)$ is the probability of a collision with isotope Z of particles at energy E and location r resulting in reaction $\mathcal{R}$.

The integral in Equation (1) is termed the optical path length, $\Lambda(E')$. The optical path length is calculated by ray-tracing from the collision point to the detector and summing the distance in each material times the total cross-section of each material at the secondary photon energy. In equation form the optical path length is:

$$\Lambda(E') = \sum_{i=1}^{N} d_i\Sigma_i(E')\,, \tag{2}$$

where d_i is the ray-trace path length in the i^{th} material, N is the number of materials in the simulation, and $\Sigma_i(E')$ is the total cross-section at energy, E', of material i. Using the notation of optical path length, Equation (1) can be simplified to

$$\phi(Z,\mathcal{R},E',r') = w\,P(Z,\mathcal{R},E,r)\,\frac{p(Z,\mathcal{R},E\rightarrow E',\mu)}{2\pi|r-r'|^2}\exp\left(-\Lambda(E')\right). \tag{3}$$

If the collision isotope and reaction is chosen through random walk and the collision isotope is isotope Z and results in reaction $\mathcal{R}$ then $P(Z,\mathcal{R},E,r)$ is unity. If the collision isotope is not Z or the collision reaction

is not $\mathcal{R}$ then $P(Z, \mathcal{R}, E, r)$ is zero. So using the random walk method $P(Z, \mathcal{R}, E, r)$ is sampled. The collision isotope and reaction can be chosen by other methods with less variance using either splitting or biasing methods. In the case of splitting

$$P(Z, \mathcal{R}, E, r) = P(Z, E, r)\, P(\mathcal{R}|Z, E)\,, \tag{4}$$

where $P(Z, E, r)$ is the probability of a collision with isotope Z of particles at energy E and location r. $P(\mathcal{R}|Z, E)$ is the probability that reaction $\mathcal{R}$ will occur given that a particle of energy E collided with isotope Z. If the collision isotope is chosen through random walk $P(Z, E, r)$ is unity for collisions with isotope Z and zero otherwise. The collision isotope can also be sampled by using splitting, or by using biasing. For splitting, the pseudo-particle can be split into a pseudo-particle for each isotope and the probability calculated from

$$P(Z, E, r) = \frac{\Sigma(Z, E, r)}{\Sigma_t(E, r)}\,, \tag{5}$$

where $\Sigma(Z, E, r)$ is the macroscopic cross section of isotope Z at energy E and location r. $\Sigma_t(E, r)$ is the total cross section at energy E and location r. The method of choosing the reaction may be different than the method from choosing the collision isotope. If reaction splitting is used each reaction is assigned a reaction probability according to

$$P(\mathcal{R}|Z, E) = \frac{\sigma_{\mathcal{R}}(Z, E)}{\sigma_t(Z, E)}\,, \tag{6}$$

where $\sigma_{\mathcal{R}}(Z, E)$ is the cross-section of reaction $\mathcal{R}$ for isotope Z at energy E and $\sigma_t(Z, E)$ is the total cross section of isotope Z at energy E.

Photon coherent scattering is highly forward peaked, and can lead to very large scores for incident particles in the direction of the tally location. To illustrated the forward peak in photon coherent scattering, the angular distribution of coherent scattering for 0.15 MeV photons on Uranium is shown in Figure 2. Since coherent scattering can be rare, this results in an unlikely event with a very large score, resulting in large variance. To avoid this situation in MCATK, the photon pseudo-particle is split into a pseudo-particle for each possible reaction instead of using the random walk sampled reaction. In this case the probability of each possible reaction is calculated by Equation (6). This splitting scheme results in many small scores from coherent scattering instead of rare large scores. Alternatively, a reaction biasing scheme could be used instead of splitting to increase the probability of coherent scattering.

For isotropic scattering or emission, the probability of the particle being emitted in any direction is $1/4\pi|r - r'|^2$, thus for isotropic reactions:

$$\frac{p(Z, \mathcal{R}_{isotropic}, E \to E', \mu)}{2\pi|r - r'|^2} = \frac{1}{4\pi|r - r'|^2} \quad \Longrightarrow \quad p(Z, \mathcal{R}_{isotropic}, E \to E', \mu) = 0.5\,. \tag{7}$$

The NEE has a notable limitation. As the distance between the collision point and the detector location goes to zero, the score contribution goes to infinity. This results in the estimator having no bound on the variance. To solve this situation, a bounding sphere is defined within which collisions or sources do not contribute to the estimator using Equation (3). Instead, the contribution to the estimator due to collisions or sources within this sphere is the volume averaged fluence within a sphere surrounding the collision point. This concept, described by Carter and Cashwell [5], is used in MCNP, where it is termed "exclusion radius" and denoted as R_o. The contribution is the average flux in a sphere of radius R_o surrounding the collision point

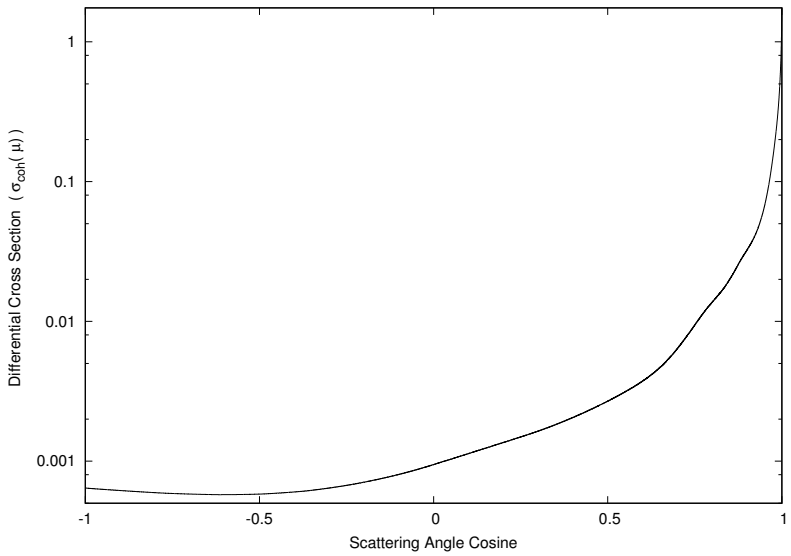

Figure 2: Photon coherent scattering differential cross section vs. angle cosine for 0.15 MeV photons on a Uranium target using `eprdata12` [2, 3, 4]. Note that the cross section is plotted using a logarithmic scale and would appear even more forward peaked when plotted using a linear scale.

$$\phi(R < R_o) = \frac{\int \phi dV}{\int dV}\,. \tag{8}$$

Substituting Equation (1) into Equation (8) yields

$$\phi(Z, \mathcal{R}, E', r' < R_o) =$$

$$w\ P(Z, \mathcal{R}, E, r)\ \frac{p(Z, \mathcal{R}, E \rightarrow E', \mu)}{2\pi}\ \frac{\int_{-1}^{1} d\mu \int_{0}^{2\pi} d\varphi \int_{0}^{R_o} r^2 dr \frac{1}{r^2} \exp\left[-\Sigma_t(E', R_o) r\right]}{\int_{-1}^{1} d\mu \int_{0}^{2\pi} d\varphi \int_{0}^{R_o} r^2 dr}\,, \tag{9}$$

which simplifies to:

$$\phi(Z, \mathcal{R}, E', r' < R_o) = w\ P(Z, \mathcal{R}, E, r)\ \frac{p(Z, \mathcal{R}, E \rightarrow E', \mu)}{2\pi}\ \frac{\int_{0}^{R_o} \exp\left[-\Sigma_t(E', R_o) r\right] dr}{\int_{0}^{R_o} r^2 dr}\,, \tag{10}$$

and results in:

$$\phi(Z, \mathcal{R}, E', r' < R_o) = w\ P(Z, \mathcal{R}, E, r)\ \frac{p(Z, \mathcal{R}, E \rightarrow E', \mu)}{2\pi}\ \frac{1 - \exp\left[-\Sigma_t(E', R_o) R_o\right]}{\frac{1}{3} R_o^3\ \Sigma_t(E', R_o)}. \tag{11}$$

This approximation assumes that *the material and density is constant* within the bounding radius. Additionally, this approximation assumes that collisions occur uniformly within the bounding radius. Uniform collisions within the sphere is necessary to provide a sampling of the probability of scatter into all angles, $p(Z, \mathcal{R}, E \rightarrow E', \mu)$. In order to accurately estimate the contribution due to collisions within the bounding radius, a sufficient sampling of collisions within the bounding sphere must occur. However, the MCNP5 physics manual [6] offers a contradiction to this logic:

> *For problems where there are many scattering events near the detector, a cell or surface estimator should be used instead of a point detector tally. If there are so few scattering events near the detector that cell and surface tallies are impossible, a point detector can still be used with a specified average flux region close to the detector.*

Photon Physics for the Next-Event Estimator

A detailed description of the implementation of photon physics models in MCATK is given in the document "Continuous Energy Photon Transport Implemented in MCATK" [7].

Photons undergo four reactions, photoelectric absorption, pair-production, incoherent scatter, and coherent scatter. Photoelectric absorption is currently modeled as absorption in MCATK and no electrons are emitted (as there is no electron transport in MCATK). Thus, no secondaries are produced and photoelectric absorption does not contribute to the photon NEE. Pair-production is modeled assuming instantaneous annihilation of the positron. The positron annihilation is modeled as the isotropic emission of two 0.511-MeV photons. Since the photons are emitted in opposite directions, the isotropic probability of scattering into a given angle cosine is doubled:

$$p_{pp}(Z, E \rightarrow E', \mu) = 2 \times 0.5 = 1.0\,. \tag{12}$$

The energy of the photons resulting from the positron annihilation are assigned the rest mass of an electron,

$$E'_{pp} = m_e c^2\,. \tag{13}$$

The electron created in pair-production is not transported.

Both incoherent (Compton) and coherent (Thomson) scattering events result in a scattered photon. For incoherent and coherent scattering the probability of scattering into a given angle cosine $p(Z, \mathcal{R}, E \rightarrow E', \mu)$ is directly calculated, not sampled. For incoherent scattering the probability of scattering into a given angle cosine is given by the ratio of the differential incoherent cross section to the total incoherent cross section,

$$p_{incoh}(Z, E \rightarrow E', \mu) = \frac{\sigma_{incoh}(Z, E \rightarrow E', \mu)}{\sigma_{incoh}(Z, E)}\,, \tag{14}$$

where $\sigma_{incoh}(Z, E, \mu)$ is the differential incoherent cross-section at angle cosine μ and $\sigma_{incoh}(Z, E)$ is the total incoherent reaction cross-section.

$$\sigma_{incoh}(Z, E) = \int_{-1}^{1} \sigma_{incoh}(Z, E \rightarrow E', \mu) d\mu\,. \tag{15}$$

The differential incoherent cross section is calculated from a modification of the differential Klein-Nishina cross-section,

$$\sigma_{incoh}(Z, E \rightarrow E', \mu) = I(Z, E, \mu)\; K(E, \mu)\,, \tag{16}$$

where $I(Z, E, \mu)$ is the incoherent form factor, and $K(E, \mu)$ is the differential Klein-Nishina cross section' [7]. The outgoing energy is based on kinematics,

$$E'_{incoh} = \frac{1}{1 + \alpha(1 - \mu)} E \,, \tag{17}$$

where α is the ratio of the incoming photon energy to the electron rest mass, $\alpha = E/(m_e c^2)$.

For coherent scattering, the probability of scattering into a given angle cosine is given by the ratio of the differential coherent cross section to the total coherent cross section,

$$p_{coh}(Z, E, \mu) = \frac{\sigma_{coh}(Z, E, \mu)}{\sigma_{coh}(Z, E)} \,, \tag{18}$$

where $\sigma_{coh}(Z, E, \mu)$ is the differential coherent cross-section at angle cosine μ and $\sigma_{coh}(Z, E)$ is the total coherent reaction cross-section.

$$\sigma_{coh}(Z, E) = \int_{-1}^{1} \sigma_{coh}(Z, E, \mu) d\mu \,. \tag{19}$$

The differential coherent cross section is calculated from a modification of the differential Thomson cross-section,

$$\sigma_{coh}(Z, E, \mu) = C^2(Z, E, \mu)\, T(\mu) \,, \tag{20}$$

where $\sigma_{coh}(Z, E)$ is the coherent cross-section, $C^2(Z, E, \mu)$ is square of the coherent form factor, and $T(\mu)$ is the differential Thomson cross section' [7]. The outgoing energy for coherent scattering is equal to the incoming energy

$$E'_{coh} = E \,. \tag{21}$$

When Equations (12), (14), and (18) are put into Equation (3) and the reaction probability is obtained from Equation (6) we obtain:

$$\begin{aligned}
\phi(Z, E \to E'_{pp}, r') &= w \frac{\sigma_{pp}(Z, E)}{\sigma_t(Z, E)} \frac{1}{2\pi |r - r'|^2} \exp\left(-\Lambda(E'_{pp})\right) \\
\phi(Z, E \to E'_{incoh}, r') &= w \frac{\sigma_{incoh}(Z, E)}{\sigma_t(Z, E)} \frac{1}{2\pi |r - r'|^2} \frac{I(Z, E, \mu) K(E, \mu)}{\sigma_{incoh}(Z, E)} \exp\left(-\Lambda(E'_{incoh})\right) \\
\phi(Z, E \to E'_{coh}, r') &= w \frac{\sigma_{coh}(Z, E)}{\sigma_t(Z, E)} \frac{1}{2\pi |r - r'|^2} \frac{C^2(Z, E, \mu) T(\mu)}{\sigma_{coh}(Z, E)} \exp\left(-\Lambda(E'_{coh})\right) .
\end{aligned} \tag{22}$$

The coherent and incoherent reaction cross-sections cancel out, thus only the pair-production and total cross-sections are required.

$$\begin{aligned}
\phi(Z, E \to E'_{pp}, r') &= w \frac{\sigma_{pp}(Z, E)}{\sigma_t(Z, E)} \frac{1}{2\pi |r - r'|^2} \exp\left(-\Lambda(E'_{pp})\right) \\
\phi(Z, E \to E'_{incoh}, r') &= \frac{w}{\sigma_t(Z, E)} \frac{1}{2\pi |r - r'|^2} I(Z, E, \mu) K(E, \mu) \exp\left(-\Lambda(E'_{incoh})\right) \\
\phi(Z, E \to E'_{coh}, r') &= \frac{w}{\sigma_t(Z, E)} \frac{1}{2\pi |r - r'|^2} C^2(Z, E, \mu) T(\mu) \exp\left(-\Lambda(E'_{coh})\right) .
\end{aligned} \tag{23}$$

These equations represent the photon pre-collision NEE at a point, as implemented in MCATK, for photon induced reactions.

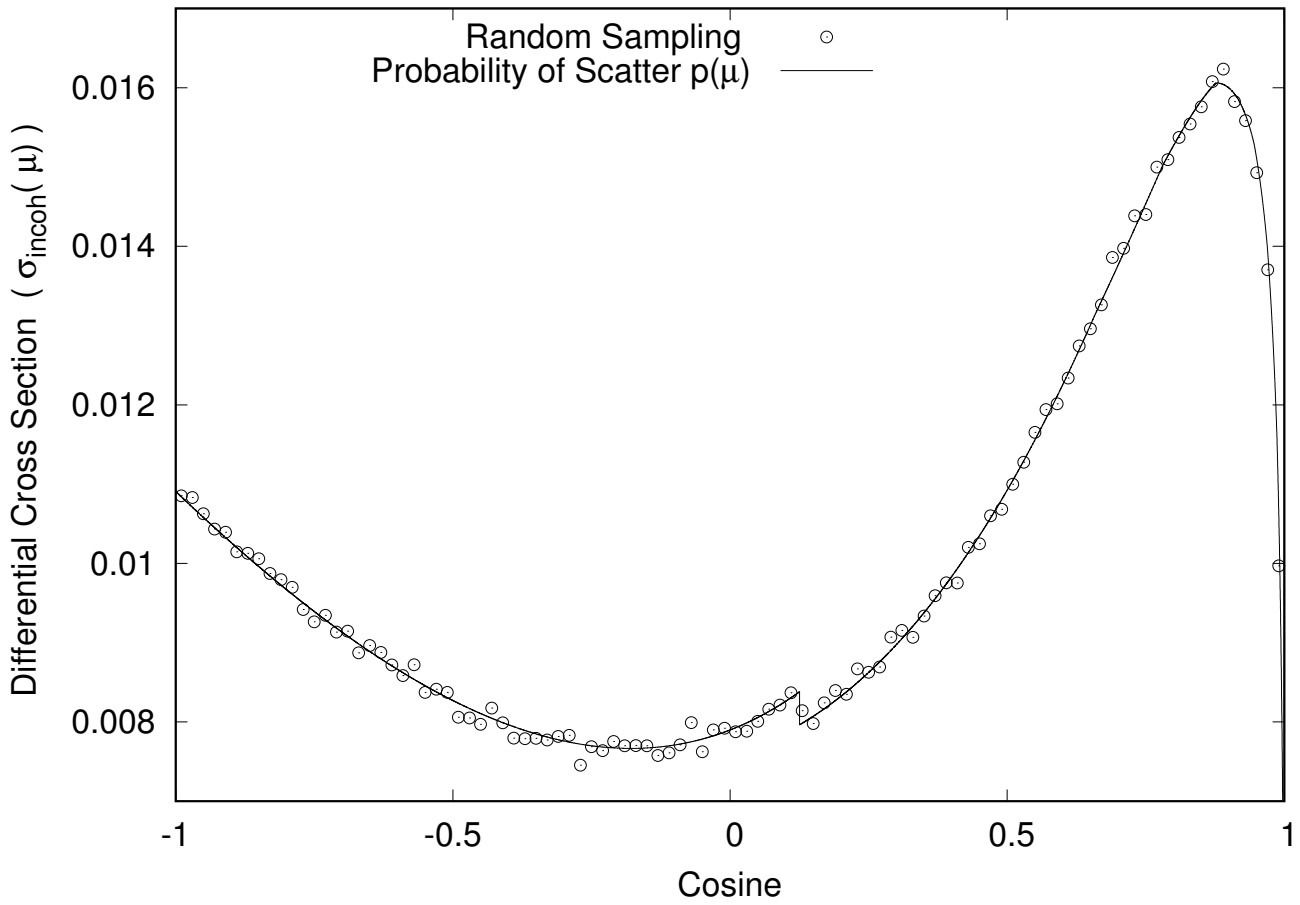

Figure 3: Comparison of the photon incoherent differential cross section as directly calculated with Equation (14) verses a histogram of the scattering angle cosine of randomly sampled incoherent events for 0.15 MeV photons incoherently scattered on Uranium using the 04p photon library. Notice that the discontinuity at a cosine of ~ 0.1, which is due to the upper bound of the form factor data in the 04p library, is preserved in both methods.

The probability of scatter into a given angle cosine for incoherent scattering, Equation (14), as implemented in MCATK, has been compared with the random walk sampling of the photon incoherent emission coinse angle. This has been done for Uranium using both the 04p (`mcplib04`) and 12p (`eprdata12`) photon libraries for a range of incident energies. Both methods agree well. An example for 0.15-MeV photons on Uranium using the 04p library is given in Figure 3. Also the probability of scatter into a given angle cosine for coherent scattering, Equation (18), as implemented in MCATK has been compared with the random walk sampling of the photon coherent emission angle cosine. Again the direct calculation and the random sampling methods are consistent. An example of the comparison of the two methods for photon coherent emission probability are given in Figure 4 for 0.15-MeV photons on Uranium using the 04p library.

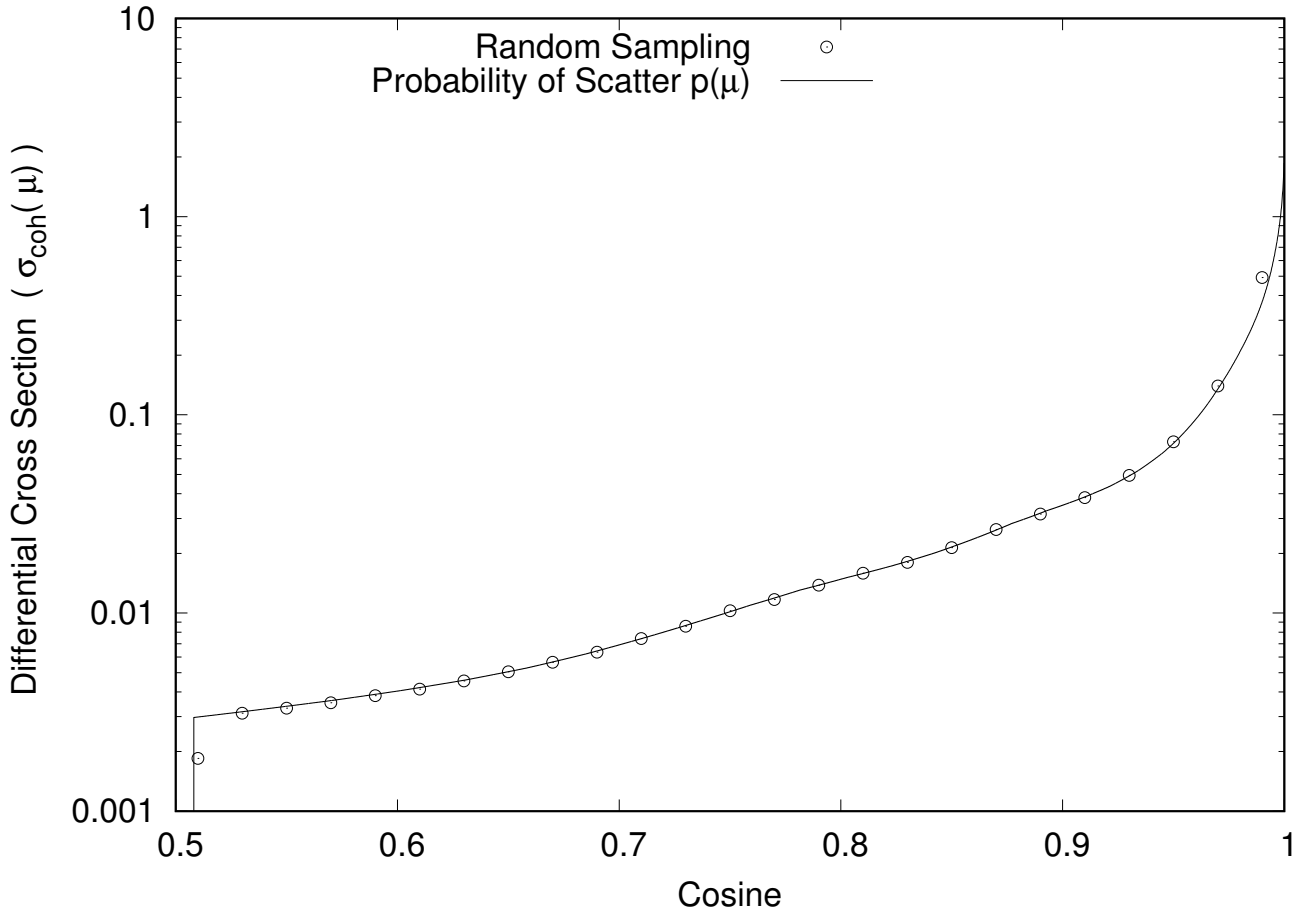

Figure 4: Comparison of the photon coherent differential cross section as directly calculated with Equation (18) verses a histogram of the scattering angle cosine of randomly sampled coherent events for 0.15 MeV photons coherently scattered on Uranium using the 04p photon library. Notice that cutoff for scattering into backward angles, which is an artifact of the older 04p library, is preserved in both methods.

Contributions to Photon Next-Event Estimators from Neutron Reactions

Neutron reactions are another source of photons which must be accounted for when estimating the photon fluence with next-event estimators. The production of photons from neutron reactions is discussed in "Continuous Energy Photon Transport Implemented in MCATK" [7]. Contributions to NEEs from photons generated by neutron reactions is calculated with Equation (3). The collision isotope and reaction is sampled randomly, so $P(Z, \mathcal{R}, E, r)$ is unity. Generally, photons from neutron reactions are modeled as being emitted isotropically, $p(Z, \mathcal{R}, E \rightarrow E', \mu) = 0.5$. There are some reactions that are modeled using a table of 32 equal probability bins (constant probability within the bin). In the case that a table is used to describe the angular distribution of the secondary photons, the probability of emission in a given direction is calculated from a table lookup. A comparison of the table lookup of the differential angular probabilities for photons generated from 20.0 MeV neutron on a carbon target is compared to a tabulation of the randomly sampled photon emission angle cosines is given in Figure 5.

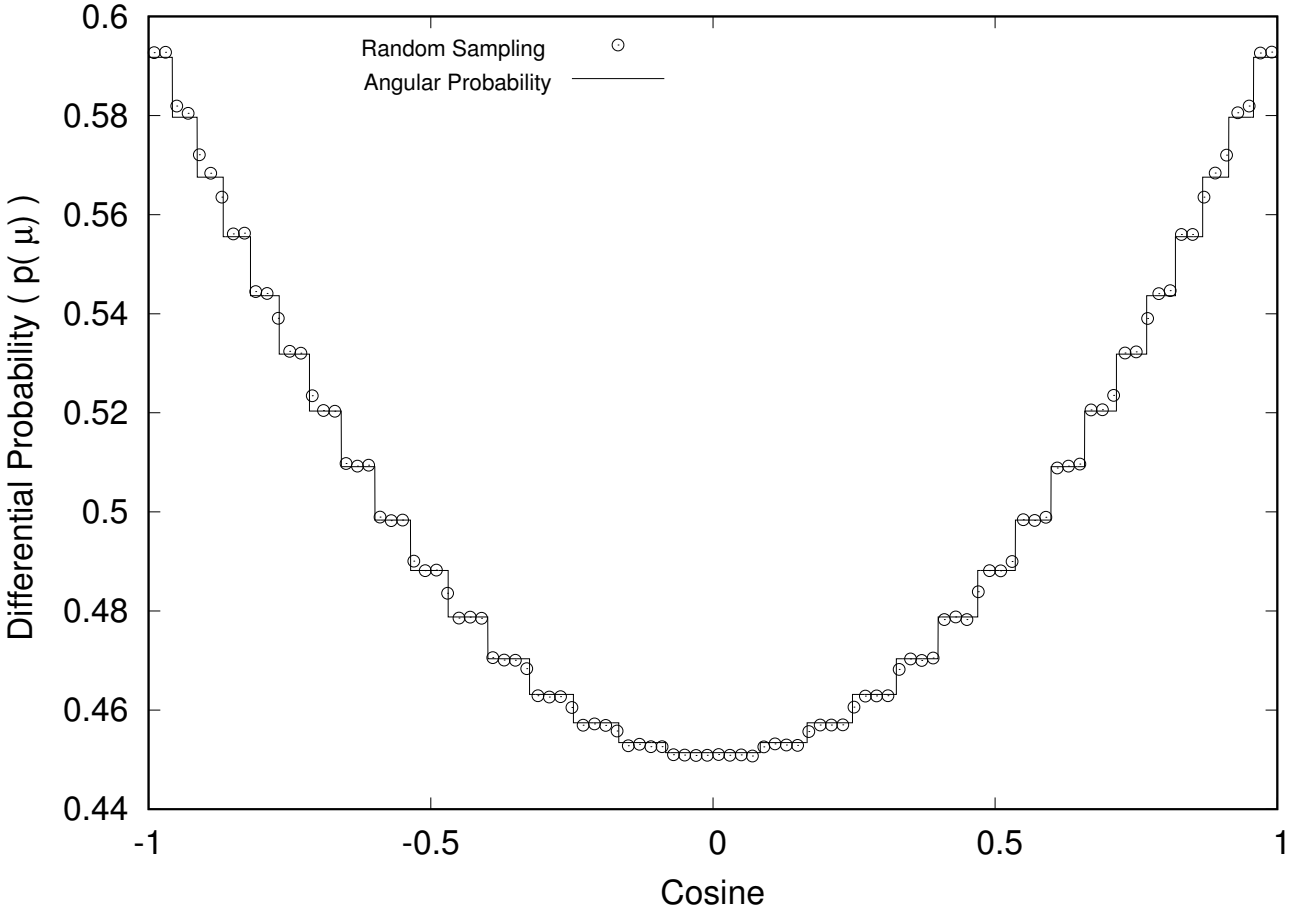

Figure 5: Comparison of the photon distribution from 20.0 MeV neutrons on carbon from a table lookup (−) verses a histogram of the scattering angle cosine of randomly sampled secondary photons (⊙) using 8000.80c ENDFB-VII cross-section data.

Implementation

The photon NEE in MCATK is implemented in the `PhotonNextEventEstimator` class which is located in the directory `src/Tallies/NextEventEstimators`. The `PhotonNextEventEstimator` class holds a vector of `pointTally` class objects. The `PhotonNextEventEstimator` class contains the mechanics of performing the next event estimation, while the `pointTally` class holds the tally information.

The photon NEE is linked with the `PhotonCollisionKernel` class with a signal/slot mechanism similiar to how track-length tallies are made. There are 3 signal / slots connecting `PhotonCollisionKernel` to `PhotonNextEventEstimator`. These 3 signal slot pairs are listed in Table 1.

Table 1: `PhotonCollisionKernel` to `PhotonNextEventEstimator` signal slot mapping.

`PhotonCollisionKernel` signal	`PhotonNextEventEstimator` slot
`PreCollisionPhotonTally_signal`	`score`
`SourceTally_signal`	`scoreSource`
`FinalizePartialTallyScores_signal`	`finalizeScore`

A `PhotonNextEventEstimator` instance is registered with the `PhotonCollisionKernel` by passing the `PhotonNextEventEstimator` instance to the templated function `PhotonCollisionKernel::connectPreCollisionPhotonTally(T& obj)`. Multiple instances of `PhotonNextEventEstimator` can be registered with the `PhotonCollisionKernel` and each `PhotonNextEventEstimator` can hold multiple instances of `pointTally`.

The `pointTally` class holds the estimator location, exclusion radius, and tally information. The tally information that is maintained are the tallies from source events, tallies from collision far from the detector, and tallies from collisions within the exclusion radius. Each individual tally can be retrieved or the total can be retrieved. The estimated standard deviation for the 3 types of events is also stored for each point.

MCATK uses a pre-collision photon NEE. This means that the three photon reactions that can produce secondaries in MCATK all result in secondaries at different energies. To avoid ray-tracing to each detector 3 times, the ray trace is performed once and the distance, d_i, in each material, i, is tallied. Then to calculate the optical path length for each secondary energy, $\Lambda(E)$, the path length in each material is folded with the cross-section of each material at the secondary photon energy, using Equation 2.

The NEE in MCATK works in parallel for domain replicated MPI. It **DOES NOT** work for domain decomposition. One can imagine the difficulty of passing multiple rays per particle history to the domain that contains the NEE location.

Testing

Three test suites have been created to test the NEE implementation in MCATK. One test suite tests the NEE in a void while the second test suite tests the NEE in material. Each of these suites contains 8 tests problems. The last suite tests ability of MCATK to calculate the source and scattered components of a simulated radiograph. The results of MCATK for the three suites of problems are compared to results from MCNP6.

Next-Event Estimator in Void Tests

The NEE was tested in a void using tests developed as an inter-code comparison between MCNP and the CEA code DIANE [8]. For this test, photons are directed down the axis of a cylinder, 400 cm long and 40 cm in diameter. A NEE is placed 400 cm off-axis at a distance of 175 cm along the axis. The geometry for this test is shown in Figure 6. Eight versions of the test are performed with different cylinder material and photon energy combinations. The material, material density, and photon energies used in each test are listed in Table 2. The material densities were set to make the cylinder approximately 7 mean free paths long in each case. The composition of each material is listed in Table 3.

The results of MCATK and MCNP6 are given in Table 4. All of the MCATK results are less than 2 standard deviations from the MCNP results except the results of Case 1. For Case 1 the differences between MCATK and MCNP are 0.065% but this difference is 6.9 standard deviations. Since the difference is on the order of 6×10^{-14}, the differences are most likely due to round-off.

Next-Event Estimator Exclusion Radius Approximation Tests

The NEE was also tested in material to exercise the exclusion radius approximation. For this test a cylinder 40 cm long and 40 cm in diameter is used. A next event estimator was placed 10 cm off axis, 10 cm from the base of the cylinder (see Figure 7). The source is located at 0.1 cm from the face of the

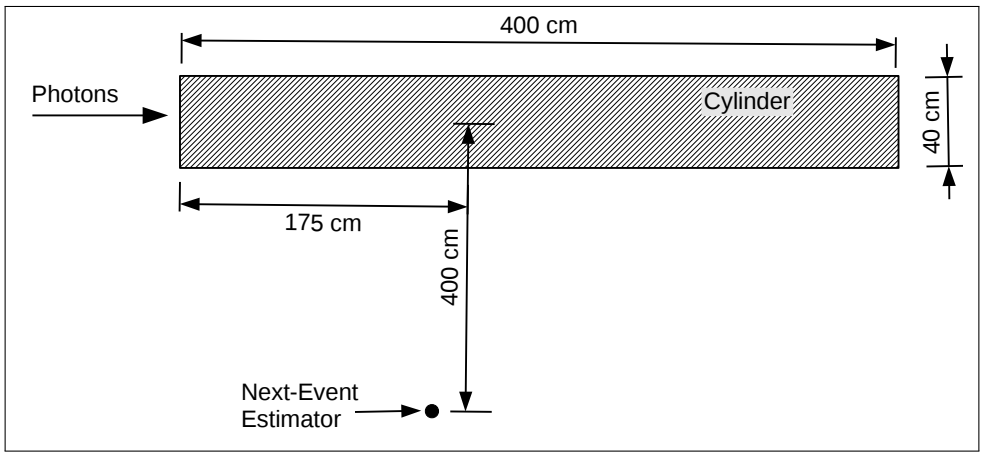

Figure 6: Diagram of the geometry of the NEE in void tests.

Table 2: Photon NEE in void tests material and photon energy specifications.

Case	Material	Density (g/cc)	Photon Energy (MeV)
1	Tungsten (W)	7.5×10^{-5}	0.003
2	Tungsten (W)	1.0×10^{-3}	0.015
3	Tungsten (W)	5.6×10^{-2}	0.13
4	Tungsten (W)	2.6	2.0
5	Tungsten (W)	2.0	60.0
6	Concrete	1.9	2.0
7	Water	1.5	2.0
8	Iron (Fe)	2.3	2.0

cylinder. The source is emitted in a conical segment between 40 and 50 degrees with respect to the cylinder axis. The source energy, cylinder material, and material densities are also listed in Table 2 and the material composition is the same as in Table 3.

The MCATK and MCNP results of the NEE in a material are listed in Table 5. Table 5 breaks down the detector response due to collisions far from the detector point "Far" and the detector response due to collisions near the detector point "Near" where the exclusion radius approximation is used. All MCATK results compare well with the MCNP results except the "Near" tally of Case 7. For Case 7 the cylinder is made of water and the photon energy is 2.0 MeV. It is unknown what is the source of the differences for Case 7. A bug in MCNP6 in the exclusion radius approximation for the pre-collision NEE was found by comparing to MCATK (in full disclosure the bug was introduced into MCNP6 in 2010 by the author of this report). The bug and fix were reported to the MCNP6 Point-of-Contact.

Table 3: Photon NEE in void tests material compositions.

Material	Isotopic ZAID	Atomic Fraction
Tungsten (W)	74184	1.0
Concrete	1001	8.4850
	8106	60.4654
	14028	24.1171
	13027	2.4875
	11022	1.2533
	20040	2.7217
	26054	0.4694
Water	1001	2.0
	8016	1.0
Iron (Fe)	26054	1.0

Table 4: Results of the photon NEE in void tests.

Case	MCATK	MCNP	Difference (MCATK-MCNP)	δ/σ
1	$8.5988 \pm 0.0006 \times 10^{-11}$	$8.6044 \pm 0.0006 \times 10^{-11}$	$-5.67 \pm 0.83 \times 10^{-14}$	-6.9
2	$3.9304 \pm 0.0011 \times 10^{-10}$	$3.9298 \pm 0.0011 \times 10^{-10}$	$6.54 \pm 15.61 \times 10^{-14}$	0.4
3	$7.7615 \pm 0.0139 \times 10^{-10}$	$7.7380 \pm 0.0136 \times 10^{-10}$	$2.35 \pm 1.94 \times 10^{-12}$	1.2
4	$8.1648 \pm 0.0261 \times 10^{-9}$	$8.1160 \pm 0.0254 \times 10^{-9}$	$4.89 \pm 3.65 \times 10^{-11}$	1.3
5	$8.0945 \pm 0.0232 \times 10^{-9}$	$8.1551 \pm 0.0235 \times 10^{-9}$	$-6.05 \pm 3.30 \times 10^{-11}$	-1.8
6	$1.5290 \pm 0.0011 \times 10^{-7}$	$1.5292 \pm 0.0011 \times 10^{-7}$	$-1.74 \pm 14.89 \times 10^{-11}$	-0.1
7	$2.5221 \pm 0.0014 \times 10^{-7}$	$2.5224 \pm 0.0014 \times 10^{-7}$	$-3.35 \pm 20.01 \times 10^{-11}$	-0.2
8	$7.6589 \pm 0.0072 \times 10^{-8}$	$7.6708 \pm 0.0072 \times 10^{-8}$	$-1.19 \pm 1.02 \times 10^{-10}$	-1.2

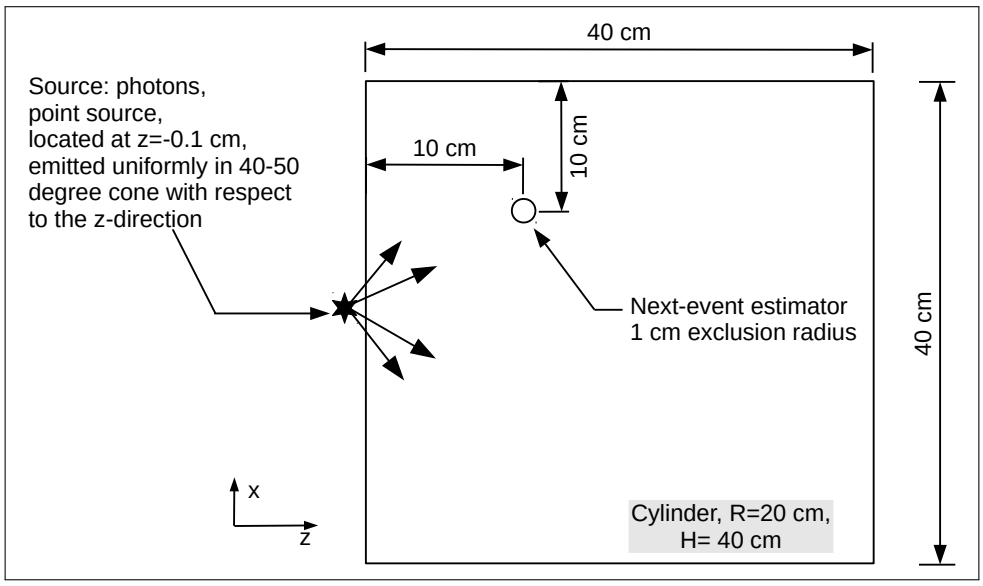

Figure 7: Diagram of the geometry for the test of the NEE exclusion radius approximation.

Table 5: Photon NEE exclusion radius approximation test results.

Case	Det.	MCATK	MCNP	Difference (MCATK-MCNP)	δ/σ
1	Near	$5.6717 \pm 0.1231 \times 10^{-7}$	$5.8015 \pm 0.1259 \times 10^{-7}$	$-1.2975 \pm 1.7606 \times 10^{-8}$	-0.7
	Far	$1.6549 \pm 0.0010 \times 10^{-6}$	$1.6621 \pm 0.0050 \times 10^{-6}$	$-7.1500 \pm 5.0910 \times 10^{-9}$	-1.4
	Total	$2.2221 \pm 0.0028 \times 10^{-6}$	$2.2422 \pm 0.0135 \times 10^{-6}$	$-2.0095 \pm 1.3741 \times 10^{-8}$	-1.5
2	Near	$2.6041 \pm 0.0349 \times 10^{-6}$	$2.5866 \pm 0.0347 \times 10^{-6}$	$1.7460 \pm 4.9184 \times 10^{-8}$	0.4
	Far	$1.0121 \pm 0.0007 \times 10^{-5}$	$1.0112 \pm 0.0015 \times 10^{-5}$	$0.9300 \pm 1.6684 \times 10^{-8}$	0.6
	Total	$1.2725 \pm 0.0017 \times 10^{-5}$	$1.2698 \pm 0.0038 \times 10^{-5}$	$2.6700 \pm 4.1855 \times 10^{-8}$	0.6
3	Near	$1.2272 \pm 0.0218 \times 10^{-5}$	$1.2553 \pm 0.0223 \times 10^{-5}$	$-2.8050 \pm 3.1247 \times 10^{-7}$	-0.9
	Far	$6.6091 \pm 0.0074 \times 10^{-5}$	$6.6079 \pm 0.0106 \times 10^{-5}$	$0.1190 \pm 1.2925 \times 10^{-7}$	0.1
	Total	$7.8363 \pm 0.0169 \times 10^{-5}$	$7.8632 \pm 0.0244 \times 10^{-5}$	$-2.6860 \pm 2.9683 \times 10^{-7}$	-0.9
4	Near	$2.1058 \pm 0.0072 \times 10^{-4}$	$2.1051 \pm 0.0072 \times 10^{-4}$	$0.0740 \pm 1.0124 \times 10^{-6}$	0.1
	Far	$5.2889 \pm 0.0048 \times 10^{-4}$	$5.2874 \pm 0.0069 \times 10^{-4}$	$1.5200 \pm 8.4000 \times 10^{-7}$	0.2
	Total	$7.3947 \pm 0.0119 \times 10^{-4}$	$7.3924 \pm 0.0096 \times 10^{-4}$	$0.2270 \pm 1.5301 \times 10^{-6}$	0.1
5	Near	$2.6448 \pm 0.0071 \times 10^{-4}$	$2.6265 \pm 0.0071 \times 10^{-4}$	$1.8320 \pm 1.0064 \times 10^{-6}$	1.8
	Far	$4.2964 \pm 0.0039 \times 10^{-4}$	$4.3005 \pm 0.0030 \times 10^{-4}$	$-4.1300 \pm 4.9113 \times 10^{-7}$	-0.8
	Total	$6.9412 \pm 0.0125 \times 10^{-4}$	$6.9270 \pm 0.0030 \times 10^{-4}$	$1.4190 \pm 1.2807 \times 10^{-6}$	1.1
6	Near	$4.0490 \pm 0.0057 \times 10^{-4}$	$4.0654 \pm 0.0057 \times 10^{-4}$	$-1.6390 \pm 0.8033 \times 10^{-6}$	-2.0
	Far	$1.1938 \pm 0.0006 \times 10^{-3}$	$1.1925 \pm 0.0002 \times 10^{-3}$	$1.2900 \pm 0.6600 \times 10^{-6}$	2.0
	Total	$1.5987 \pm 0.0015 \times 10^{-3}$	$1.5991 \pm 0.0006 \times 10^{-3}$	$-0.3500 \pm 1.6036 \times 10^{-6}$	-0.2
7	Near	$4.2003 \pm 0.0042 \times 10^{-4}$	$4.1728 \pm 0.0042 \times 10^{-4}$	$2.7480 \pm 0.5921 \times 10^{-6}$	4.6
	Far	$1.3235 \pm 0.0006 \times 10^{-3}$	$1.3228 \pm 0.0003 \times 10^{-3}$	$6.9000 \pm 6.9886 \times 10^{-7}$	1.0
	Total	$1.7436 \pm 0.0015 \times 10^{-3}$	$1.7401 \pm 0.0005 \times 10^{-3}$	$3.5000 \pm 1.5826 \times 10^{-6}$	2.2
8	Near	$3.4689 \pm 0.0062 \times 10^{-4}$	$3.4690 \pm 0.0062 \times 10^{-4}$	$-0.1200 \pm 8.8305 \times 10^{-7}$	0.0
	Far	$9.4689 \pm 0.0056 \times 10^{-4}$	$9.4795 \pm 0.0066 \times 10^{-4}$	$-1.0630 \pm 0.8686 \times 10^{-6}$	-1.2
	Total	$1.2938 \pm 0.0014 \times 10^{-3}$	$1.2949 \pm 0.0009 \times 10^{-3}$	$-1.0600 \pm 1.6495 \times 10^{-6}$	-0.6

Radiographic Test Object

The NEE is workhorse of computational radiography. In order to test NEEs in MCATK for use in simulated radiography, the Radiographic Test Object [9], RTO, was simulated and results where compared with MCNP. The RTO was developed to help diagnostic users ensure the proper alignment. A rendering of the RTO is given in Figure 8. The direct source only (without scattering) radiograph of the RTO simulated with MCATK and MCNP are given in Figures 9(a) and 9(c) respectively. The difference between the MCATK and MCNP direct source radiographs is given in Figure 9(e). For this simulation, MCATK and MCNP calculate the same value for 89.2% of the pixels. No pixel differences exceed 0.01%. The number of pixels that are different are tallied at the 0.002%, 0.004%, and 0.006% levels and given in Table 6.

Table 6: RTO source only MCATK - MCNP differences.

Difference Range	(%) of Pixels
difference = 0.000%	89.2
0.000% < difference < 0.002%	2.0
0.002% ≤ difference < 0.004%	4.1
0.004% ≤ difference < 0.006%	4.6
difference ≥ 0.006%	0.1

The scattered contributions to the simulated radiograph are shown in Figures 9(b) and 9(d), as calculated by MCATK and MCNP respectively. The differences, in terms of number of standard deviations, in the scattered contributions calculated by MCATK and MCNP is shown in Figure 9(f). The MCATK and MCNP scattered components are statistically identical. No pixels exceed 1.5 standard deviations, with 90% of the pixels differing less than one standard deviation.

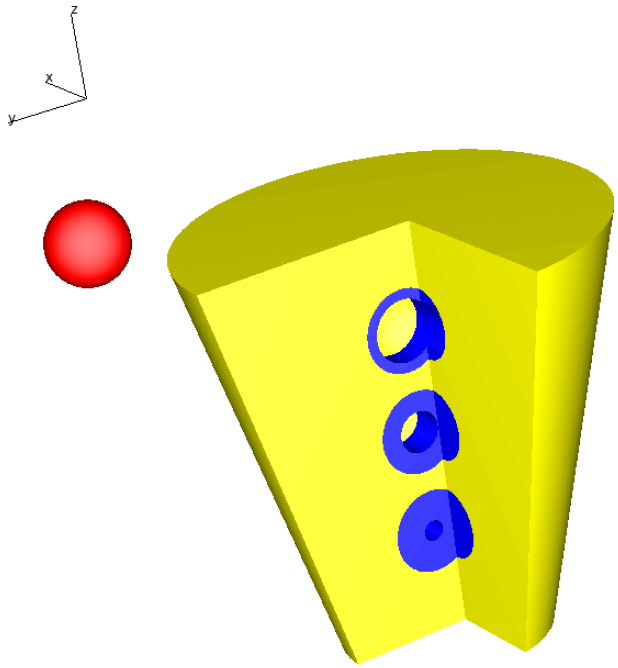

Figure 8: Rendering of the RTO.

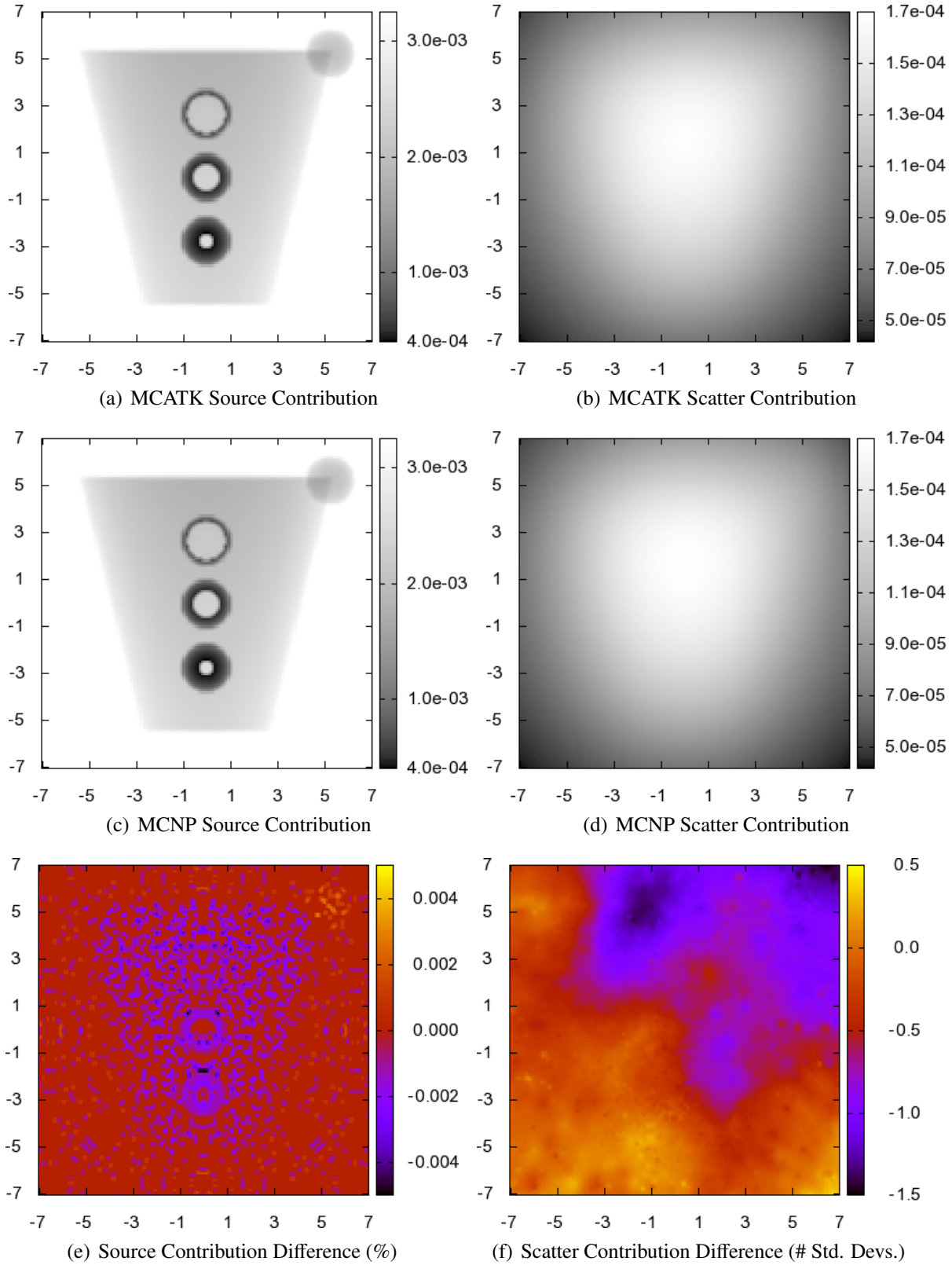

(a) MCATK Source Contribution

(b) MCATK Scatter Contribution

(c) MCNP Source Contribution

(d) MCNP Scatter Contribution

(e) Source Contribution Difference (%)

(f) Scatter Contribution Difference (# Std. Devs.)

Figure 9: Simulated radiograph components of the RTO calculated by MCATK and MCNP.

Table 7: Gamma leakage from Godiva, MCATK and MCNP results.

	MCNP $(1/cm^2)$	MCATK $(1/cm^2)$	Difference (# std. devs.)
Direct	$0.6961 \pm 0.0017 \times 10^{-8}$	$0.6977 \pm 0.0018 \times 10^{-8}$	0.98
Collided	$0.3563 \pm 0.0040 \times 10^{-8}$	$0.3603 \pm 0.0029 \times 10^{-8}$	0.92
Total	$1.0523 \pm 0.0036 \times 10^{-8}$	$1.0580 \pm 0.0034 \times 10^{-8}$	1.25

Photons from Neutron Reactions produced in Godiva

In order to test the proper functioning of the photon NEE for photons generated from neutrons, a test to measure the photon leakage from the Godiva subcritical was setup in both MCATK and MCNP6. A point detector was placed 1000 cm from the center of the Godiva assembly. The results are given in Table 7. MCNP6 was modified to count secondary photons from neutron reactions as contributing to the "Direct" component, while counting the secondary photons from photon reactions as contributing to the "Collided" component . The results of MCATK and MCNP agree.

Criticality Accident Monitor Scenario

A criticality accident scenario has been used to test the proper functioning of a time binned NEE. The criticality accident geometry was a sphere containing a uranium water mixture. The uranium water mixture was 25% uranium by weight and the uranium consisted of 10% enriched uranium. The radius of the sphere was 35 cm with a density of 1.4 g/cc. The problem was simulated with MCATK's time dependent solution mode, using a time step of 10,000 shakes. A photon NEE was placed at 1 light-second (2.998×10^{10} cm) from the center of the sphere. The simulation starts at a temperature of 20 °C. Temperature is added uniformly to the system from fission at 178 MeV per fission assuming a specific heat of 4.1813 $J/(g \cdot K)$. The system radius is held constant. The system shuts its self down mainly due to doppler broadened elastic scattering, but doppler broadening of other reactions also plays a minor role, so MCATK's multi-temperature continuous energy cross section capability is used for the simulation.

The time evolution of the fission rate is plotted along with the response of the photon NEE in Figure 10. The fission rate is time shifted by one second to align with the delayed response of the photon detector positioned at 1 light second. The response of the photon NEE is scaled to provide the same area under the curve. The results of the photon NEE match the fission rate. This simulations shows how the NEE can be used to estimate the response of time-of-flight detectors placed some distance from the experiment of interest.

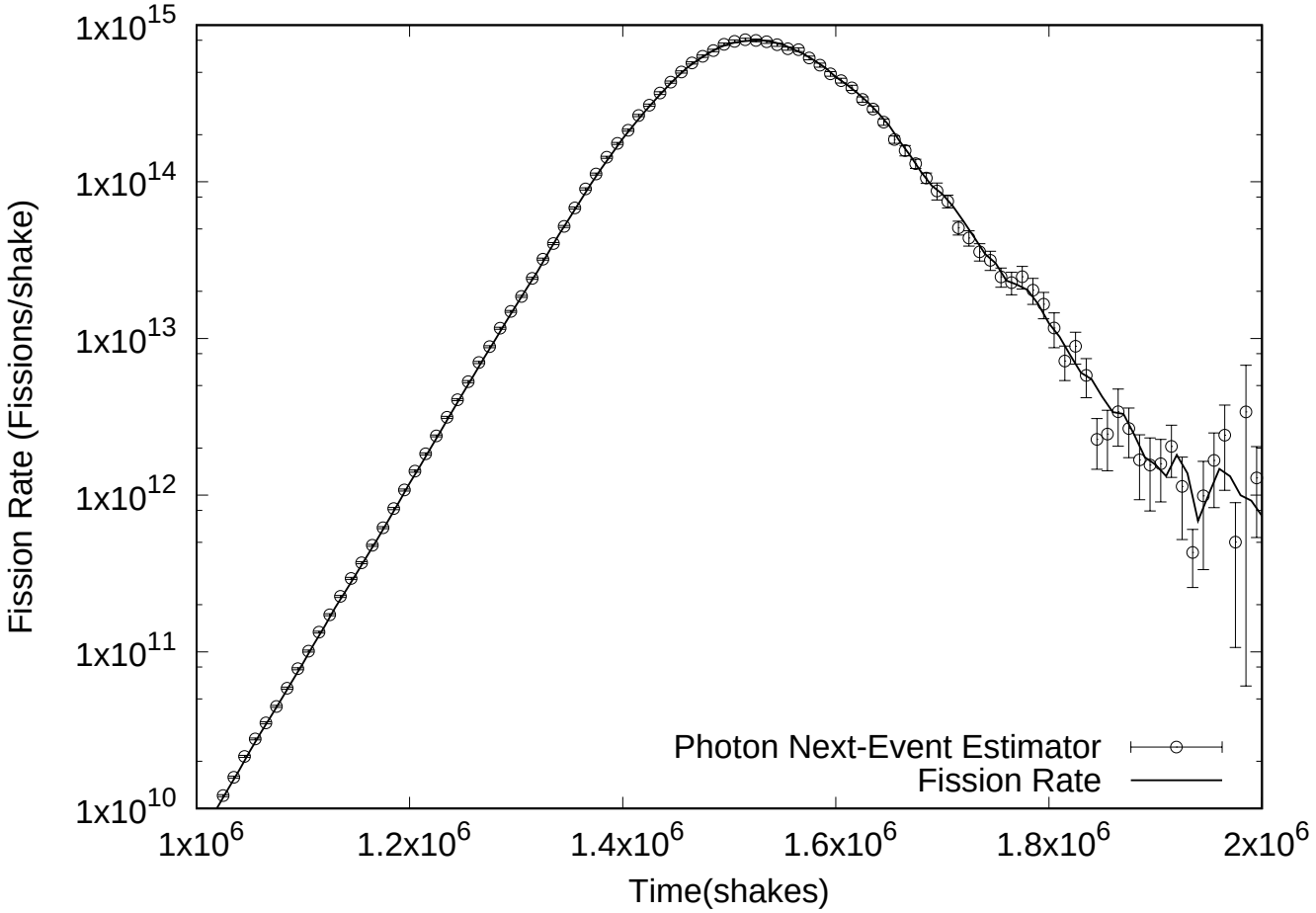

Figure 10: Comparison of the fission rate during a criticality accident scenario and the response of a photon NEE located 1 light second from the assembly. The fission rate has been shifted one second and the response of the photon NEE has been scaled to provide the same area under the curve.

References

[1] M.H. Kalos. "On the Estimation of Flux at a Point by Monte Carlo". In: *Nucl. Sci. Eng.* 16 (1963), p. 111.

[2] H.G. Hughes. *"Enhanced Electon-Photon Transport in MCNP6"*. Tech. rep. LA-UR-13-27632. Los Alamos National Laboratory, 2013.

[3] H.G. Hughes. *"An Electron/Photon/Relaxation Data Library for MCNP6"*. Tech. rep. LA-UR-13-27377. Los Alamos National Laboratory, 2013.

[4] H.G. Hughes. *"Enhanced Electon-Photon Transport in MCNP6"*. Tech. rep. LA-UR-13-27378. Los Alamos National Laboratory, 2013.

[5] L.L. Carter and E.D. Cashwell. *Particle-Transport Simulation with the Monte Carlo Method*. TID-26607. Springfield, Virginia: National Technical Information Service, Oct. 1975. DOI: 10.2172/4167844. URL: http://www.osti.gov/scitech/servlets/purl/4167844.

[6] X-5 Monte Carlo Team. *MCNP - A General Monte Carlo N-Particle Transport Code, Version 5, Volume I: Overview and Theory*. Technical Report LA-UR-03-1987. Los Alamos, NM, USA: Los Alamos National Laboratory, Apr. 2003 (Revised 2/1/2008). URL: https://laws.lanl.gov/vhosts/mcnp.lanl.gov/pdf_files/la-ur-03-1987.pdf.

[7] T. Adams et al. *"Continuous Energy Photon Transport Implemented in MCATK"*. Report LA-UR-16-XXXXX. Los Alamos, NM: Los Alamos National Laboratory, 2016. URL: http://permalink.lanl.gov/object/tr?what=info:lanl-repo/lareport/LA-UR-16-XXXXX.

[8] S. LeMaire, M. Caillaud, S. Menard, et al. "Radiographie et intercomparaisons de codes / Computational radiography and cross code comparisons". In: *Chocs Focus: 10 years of the CEA/DAM - DOE/NNSA Agreement* 3 (June 2012), pp. 42–43. URL: http://www-physique-chimie.cea.fr/science-en-ligne/docs/chocs-focus/Focus_n3.pdf.

[9] E. Shores, C. Solomon, J. Zumbro, D. Flamig, and Guillermo Terrones. *Radiographic Test Problem for MCNP and Other Mesh-Based Applications*. Technical Report LA-UR-12-24562. Los Alamos, NM: Los Alamos National Laboratory, 2012.

Appendix A MCNP Input for Next-Event Estimator Test in Void

```
W test for point detector
c
c Inspired from: T. Booth and D. Verwaerde, "Benchmark Calculations", in Monte-Carlo
c Methods and Applications in Neutronics, Photonics and Statistical Physics,
c R. Alcouffe, R. Dautray, A. Forster, G. Ledanois and B. Mercier, eds.,
c Springer-Verlag, Berlin (1985), p.432.
c
c
10 1 -7.5e-5 -10        $ cylinder
15 0 -30                    $ tally torus
20 0 10 -20 30              $ void
30 0 20                     $ outside

10 RCC 0 0 0 0 0 400 20         $ cylinder
20 RCC 0 0 -200 0 0 700 500     $ enclosing cylinder
30 TZ  0 0 175  400 1.0 1.0     $ tally torus

imp:p 1 1 1 0
unc:p 0 0 0 0
mode p
cut:p j 0.001
sdef par=2 pos=0 0 -0.00001  dir=1 vec=0 0 1 erg=.003 ara=1.0
c
m1 74000.12p 1.0 $ W
c
c
f4:p   15
f5:p   400         0           175 1 $   0 degrees
ft5 pds 1
c
nps 1e7
prdmp j j 1 4
print
dbcn 49j 2 1
phys:p j 1 0 j 1
```

Appendix B MCNP Input for Next-Event Estimator Test in Material

```
W test for point detector exlusion radius
10 1 -7.5e-5  -10  40     $ cylinder
20 1 -7.5e-5  -40         $ track length tally
40 0           10 -20     $ void
50 0           20         $ outside

10 RCC 0 0 0 0 0 20 20         $ cylinder
20 RCC 0 0 -200 0 0 700 500    $ enclosing cylinder
30 TZ  0 0 10 10 0.001 0.001   $ tally torus
31 TZ  0 0 10 10 0.01 0.01     $ tally torus
32 TZ  0 0 10 10 0.1 0.1       $ tally torus
40 S  10.0 0.0 10.0 1.0        $ tally sphere

imp:p 1 1 1 0
unc:p 0 0 0 0
mode p
cut:p j 0.001
c
c Source
sdef par=2 pos=0 0 -0.1  dir=d1 vec=0 0 1 erg=.003 ara=1.0
si1 0.64278761 0.766044443 1.0 $ 40-50 degrees
sp1          0           1   0
c
c Material
m1 74000 1.0 plib=04p $ W
c
dd2 0 0
c
f5:p  10         0           10 1.0 ND $   0 degrees
ft5 pds 1 icd
fu5 10 20
tf5 j j 1
c
f25:p  10         0           10 1.0 ND $   0 degrees
ft25 pds 1 icd
fu25 10 20
tf25 j j 2
c
nps 1e9
prdmp 1e9 1e9 1 j 1e8
print
dbcn 49j 2 1
phys:p j 1 0 j 1
```